Microporous and Mesoporous Materials 352 (2023) 112478

Contents lists available at ScienceDirect

Microporous and Mesoporous Materials

journal homepage: www.elsevier.com/locate/micromeso

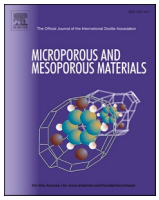

Effect of surface functionalization on the moisture stability and sorption properties of porous boron nitride

Anouk L'Hermitte [a,b], Hassan Azzan [a], Marcus H.N. Yio [c], Ashwin Kumar Rajagopalan [d,e], David Danaci [a], Takuya Hirosawa [f], Toshihiro Isobe [f], Camille Petit [a,*]

[a] Barrer Centre, Department of Chemical Engineering, Imperial College London, London, SW7 2AZ, UK
[b] Department of Materials, Imperial College London, London, SW7 2AZ, UK
[c] Centre for Infrastructure Materials, Department of Civil and Environmental Engineering, Imperial College London, London, SW7 2AZ, UK
[d] Department of Chemical Engineering, Imperial College London, London, SW7 2AZ, UK
[e] Department of Chemical Engineering, The University of Manchester, Manchester, M13 9PL, UK
[f] Department of Materials Science and Engineering, School of Materials and Chemical Technology, Tokyo Institute of Technology, Tokyo, 152-8552, Japan

ARTICLE INFO

Keywords:
Boron nitride
Porosity
Adsorption
Surface functionalization
Hydrolytic stability

ABSTRACT

Porous boron nitride (BN) is a promising adsorbent owing to its high surface area and porosity, as well as thermal and oxidative stability. It has been explored in the past decade for applications in gas and liquid separations, such as CO_2 capture and water cleaning. However, the material has displayed hydrolytic instability. Owing to the presence of moisture in most industrial settings, whether it is for storage or cyclic adsorption processes, ensuring the moisture stability of an adsorbent is crucial. While this topic has been researched for other adsorbents such as zeolites and metal organic frameworks (MOFs), little is known on controlling the hydrolytic stability of porous BN. In this study, we propose a method to enhance porous BN's hydrolytic stability via surface functionalization using a fluoroalkylsilane. We explored two different routes of functionalization: (i) functionalization of porous BN powder followed by pelletization (route 1) and (ii) coating of porous BN pellets with fluoroalkylsilane (route 2). Spectroscopic, analytical and imaging techniques confirmed the functionalization process qualitatively and quantitatively. We subjected the functionalized samples to moisture exposure at 54% RH (similar to common storage conditions) and 92% RH (similar to flue gas stream conditions with high moisture content), and characterized them to probe their resistance to moisture. We also investigated their equilibrium and kinetic sorption properties in the context of CO_2/N_2 separation. Both routes produced materials with enhanced moisture stability. However, we noted differences between both functionalization routes. Route 2 produced a sample with a higher grafting yield and hydrophobic nature, and therefore better resistance to moisture exposure than route 1. From a sorption point of view, despite reduced porosity, the functionalized samples maintain reasonable CO_2 uptakes. The functionalization led to changes in the textural features of the samples, which caused differences in the mass transfer. This work shows that functionalization could be used to protect porous BN upon moisture exposure.

1. Introduction

In the field of adsorption-based separations, porous boron nitride (BN) has proven promising as an adsorbent owing to a high surface area, high porosity, and great thermal and oxidative stability [1–3]. It has successfully been tested at laboratory scale for gas separations, such as CO_2 capture [3,4], CO_2/CH_4 separation [1], paraffin/olefin separation [5] and H_2 storage [6,7]. In the liquid phase, water cleaning has been carried out using porous BN materials for inorganic and organic pollutants removal, such as oils and dyes [6,8,9].

Looking at the nature of most separations, it appears crucial to have adsorbents that sustain water or moisture exposure during storage, transport and use. Past studies have reported the cyclic use of porous BN as adsorbent in potentially mild or extreme humidity conditions, but the impact on surface area, porosity and sorption performance upon moisture exposure was not assessed [5]. This is all the more important since studies have pointed towards the instability of porous BN in the presence of water or moisture [10–16]. Considering the potential of porous BN as an adsorbent, it is key to enhance its hydrolytic stability.

Hydrolytic instability has already been highlighted for classes of

* Corresponding author.
E-mail address: camille.petit@imperial.ac.uk (C. Petit).

https://doi.org/10.1016/j.micromeso.2023.112478
Received 9 December 2022; Received in revised form 27 January 2023; Accepted 2 February 2023
Available online 13 February 2023

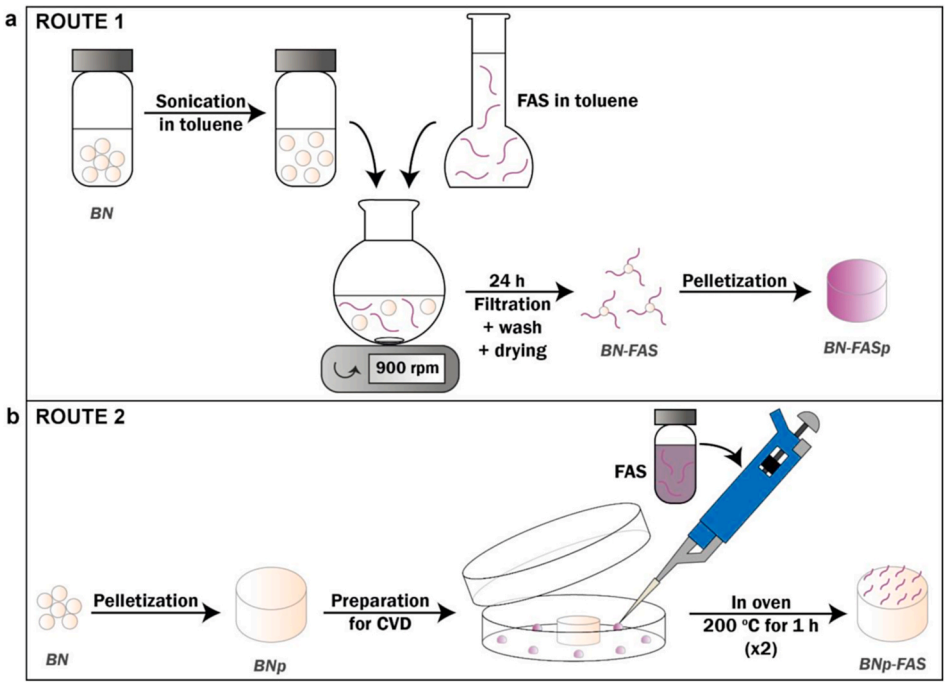

Fig. 1. Schematics representing the two experimental routes used to functionalize the surface of porous BN. (a) Experimental route 1 consisting of silylation using trimethoxy(3,3,3-trifluoropropyl)silane (FAS) followed by pelletization. (b) Experimental route 2 consisting of pelletization followed by chemical vapor deposition (CVD) using FAS.

inorganic and organic adsorbents, such as zeolites [17,18] and metal organic frameworks (MOFs) [19–24]. To tackle this limitation, methods involving surface functionalization have been used to reduce the interaction of the adsorbent with water and prevent its degradation over time and repeated use. For instance, zeolites have been functionalized via the grafting of alkylsilanes onto their OH groups [25–27], whereas MOFs have been coated with a hydrophobic polymer, like polydopamine [28]. With the right experimental conditions and chemicals, such methods allow to make these adsorbents more hydrophobic and resistant to water, while retaining adequate surface area for adsorption applications [25,26,28].

Past studies have looked at making porous BN materials more crystalline or with fewer micropores to enhance their resistance to moisture [14,15], thus reducing their surface area and sorption properties. Herein, we have looked at an alternative way to achieve a compromise between high surface area and enhanced hydrolytic stability in porous BN. Using the findings of past studies, we and others have hypothesized that the origin of the hydrolytic instability in porous BN materials derives from a combination of a lack of crystalline structure [15] and the presence of oxygen atoms, both in the bulk and at the edges of the BN sheets [14,29]. These oxygen impurities, which account for 8–9% of the atomic composition of porous BN [29], constitute hydrophilic sites in the structure that promote interaction with water, and can lead to subsequent degradation of the material following reaction (1):

$$2\,BN_{(s)} + 3\,H_2O_{(l)} \rightarrow B_2O_{3\,(s)} + 2\,NH_{3(g)} \quad (1)$$

To address this, we have functionalized the surface of porous BN similarly to other materials, such as zeolites [26,27]. We have used an alkylsilane to graft onto the OH groups present at the edges of porous BN. We have selected a fluoroalkylsilane with a short alkyl chain to benefit from the hydrophobicity of the fluorine atoms, while avoiding bulky chains that would block pores and compromise the adsorption capacity of porous BN after functionalization. We have trialed two different functionalization routes using the same silane: route 1 relies on the silylation of porous BN powder, followed by pelletization; route 2 starts with porous BN pellets, which are then subjected to chemical vapor deposition (CVD). To monitor the changes in hydrophobicity, we have subjected samples to different levels of humidity, relevant to storage and post-combustion CO_2 capture sorption testing conditions. We have then used a range of spectroscopic and analytical tools to probe the impact of moisture on the chemical and textural properties, before and after surface functionalization. Finally, we have tested the potential of our functionalized adsorbents for CO_2/N_2 separation by carrying out both equilibrium and kinetics sorption measurements.

2. Experimental section

Some of the methods described below have been used in our previous study on porous BN [29].

2.1. Synthesis of porous BN powder

The reagents boric acid (ACS reagent, Sigma Aldrich), melamine (99%, Sigma Aldrich) and urea (molecular biology grade, Sigma Aldrich) were used with molar ratios of 1:1:5 following the multiple N-precursor synthesis previously developed in our group [2]. The three precursors were physically ground and mixed for 3 min until homogeneous, before being placed in an alumina crucible with the lid partially open to allow for any gas flow. The crucible was placed inside a horizontal tubular furnace (HST 12/600, Carbolite) in N_2 flow (99.998%, zero grade, BOC). Each synthesis started with a 2 h purge at room temperature under N_2 with a flow rate of 250 $cm^3\,min^{-1}$. After this step, the flow rate was lowered to 50 $cm^3\,min^{-1}$ and the temperature ramped up to 1050 °C at a rate of 10 °C min^{-1}. The complete synthesis of the porous BN material was obtained after a dwell time of 3 h at 1050 °C before cooling down, still under flowing N_2. Samples were stored in a desiccator at room temperature without vacuum until characterization.

2.2. Pelletization of porous BN powder

40 mg of porous BN powder were ground with a mortar and pestle, and placed into a pellet die (5 mm evacuable stainless steel, Specac). The

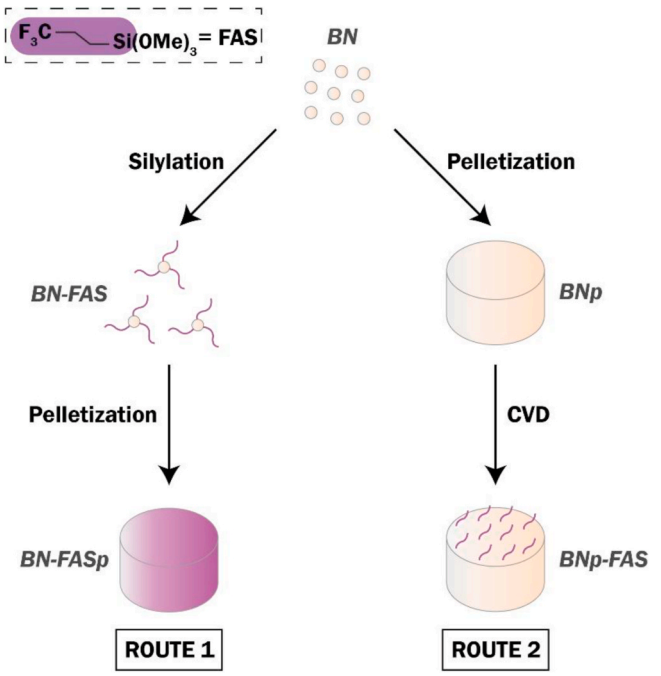

Fig. 2. Summary of experimental routes 1 and 2 used to functionalize porous BN and associated samples names.

die was positioned into a manual hydraulic press (Atlas™ Manual 15T, Specac) fitted with a low tonnage gauge conversion kit (0–1 t, Specac). A load of 0.2 t was applied and maintained for 20 s to form a pellet. The pellet was then ejected with a small load applied to an extractor ring placed onto the base of the pellet die. We observed that 0.2 t was the optimal load for successful pelletization of 40 mg porous BN while maintaining high BET area compared to porous BN powder: 1455 $m^2 g^{-1}$ and 1521 $m^2 g^{-1}$ respectively (Fig. S1).

2.3. Surface functionalization of porous BN

To make porous BN more hydrophobic, its surface was functionalized via two experimental routes using trimethoxy(3,3,3-trifluoropropyl)silane (97%, Sigma-Aldrich, CAS 429-60-7), abbreviated as FAS for fluoroalkylsilane (Fig. 1).

2.3.1. Route 1: silylation of porous BN powder followed by pelletization

We first dispersed 200 mg of porous BN powder (as synthesised following the method in section 2.1) in 4 mL of toluene (100%, ACS reagent, VWR) for 20 min in a sonicator (Clifton). In parallel, we prepared a solution of FAS in 10 mL of toluene with a concentration of 10 mmol of FAS per g of BN, hence a volume of 384 μL of FAS. The dispersed porous BN and the FAS solution were both added inside a 50-mL round-bottom flask with a magnetic stirrer. The mixture was stirred at 900 rpm at room temperature for 24 h. The resulting material was filtered and washed with ethanol (99.95%, ACS reagent, VWR) before being dried in an oven at 120 °C overnight, as shown in Fig. 1a. A control sample was prepared using the same method without FAS to check the impact of filtration, washing and drying in route 1. In a second stage, pellets were prepared with the functionalized powder following the pelletization method explained in section 2.2.

2.3.2. Route 2: chemical vapor deposition (CVD) on porous BN pellets

A pellet was prepared from 40 mg of porous BN powder following the pelletization method outlined in section 2.2. This pellet was then placed on one of its flat surfaces in the centre of a Petri dish, as shown in Fig. 1b [30]. To target 10 mmol per g of BN as in route 1 and bearing in mind we wanted to functionalize both sides of the pellet equally, 38.2 μL of pure FAS (not diluted in any solvent) were first added in several droplets around the 40-mg pellet with a volume-adjustable pipette. The lid was then placed on top of the bottom part of the Petri dish and placed in an oven at 200 °C for 1 h to carry out chemical vapor deposition (CVD). The CVD process was repeated once after delicately turning the pellet upside down in the Petri dish and adding another 38.2 μL of FAS around the pellet.

2.3.3. Glossary

We introduced a naming system for all samples (Fig. 2). This system considers the order of experimental steps carried out, such as pelletization ("p") and functionalization with FAS ("-FAS"). A control sample ("-control") was added to check the potential impact of solvents used in route 1, without using FAS. This control sample underwent each step used in route 1, but no FAS was added in the toluene solution (Fig. 1a).

2.4. Moisture exposure

Water contact angles were carried out using a Krüss Drop Shape Analyzer (DSA 25) instrument by means of sessile drop method to quickly assess hydrophobicity of the unmodified and functionalized pellets. A pellet was placed on the sample platform and a 2-mL droplet of deionized water (18 MΩ cm) was formed using a syringe controlled by the software Krüss Advance. The platform was moved up manually to bring the top surface of the pellet towards the droplet. Once the droplet was in contact with the pellet, the platform was slowly lowered down. Contact angles were then measured over 10 s with a frequency of 10 s^{-1} on two different spots of each flat surface of the pellet, hence four measurements per pellet. Short videos were also recorded with the software when the surfaces were too hydrophilic to measure static contact angles.

To investigate the impact of humidity exposure on the samples in more depth, we set up a closed environment with a plastic box and its lid sealed with vacuum grease (Fig. S2). A beaker was filled with a saturated salt solution and placed inside the sealed box. A sample was then placed inside the box and subjected to a given relative humidity (RH) level for 24 h in a temperature-controlled environment. 24 h was selected as the exposure time for two reasons: this is a relatively short time for industrial purpose, and significant impact had been observed on a similar material in a past study for exposure at relative humidity above 90% for 8 h [14]. Relative humidity can be fixed with a given saturated salt solution at a set temperature [31]. We used two different salts to prepare saturated solutions: magnesium nitrate and potassium nitrate. At 22 °C, these two saturated solutions produce RH levels of 54% and 92% respectively. These RH values could correspond to two industrial scenarios: 54% represents a RH level that can be found in storage conditions, whereas 92% represents more extreme conditions that can be seen in some adsorption processes, such as CO_2 capture with high moisture content [32]. After humidity exposure, samples were dried in a vacuum oven overnight at 110 °C.

To obtain additional insight into the behavior of unmodified and functionalized porous BN upon moisture exposure, water vapor sorption isotherms were collected using a Micromeritics 3Flex porosity analyzer at 22 °C. Deionized water was placed in a container fitted to the instrument and purified with 4 freeze-pump-thaw cycles prior to the measurement to remove any air and dissolved gases. All samples were first degassed ex-situ overnight at 140 °C and 0.2 mbar and then degassed in-situ at 120 °C for 4 h at 0.0030 mbar.

2.5. Materials characterization

2.5.1. Chemical features

Samples were analyzed using Fourier transform infrared (FTIR) spectroscopy. Each powder sample was ground finely in an agate mortar and spectra were collected using an Agilent Cary 630 FTIR spectrometer equipped with an attenuated total reflectance (ATR) accessory.

Pelletized samples were analyzed without prior treatment. Sixteen spectra were collected per sample to obtain an averaged spectrum over a wavenumber range of 450–4000 cm^{-1} with a resolution of 2 cm^{-1}.

X-ray photoelectron spectroscopy (XPS) analyses were performed using a Thermo Scientific K-Alpha X-ray photoelectron spectrometer equipped with an MXR3 Al Kα monochromatic X-ray source ($h\nu$ = 1486.6 eV) set to 72 W (6 mA and 12 kV). Powder samples were ground in an agate mortar prior to analysis and mounted onto carbon tape. Pelletized samples were directly mounted onto carbon tape. The data was processed with Thermo Scientific Avantage™ software for B 1*s*, N 1*s*, O 1*s*, C 1*s*, Si 2*s*, Si 2*p* and F 1*s* spectra. The adventitious carbon (C–C) peak set at 284.8 eV was used for binding energy calibration.

Thermogravimetric analysis (TGA) was carried out with a Netzsch TG 209 F1 Libra thermal analyzer for porous BN powder and the functionalized samples. Powder samples were ground prior to measurement and pelletized samples were directly placed in an alumina crucible. The heat treatment first consisted of heating from room temperature to 120 °C and maintaining this temperature for 30 min to remove any moisture. The temperature was then increased to 800 °C with a ramp rate of 10 °C min^{-1} under a mixture of air flow (80 mL min^{-1}) and protective N_2 flow (20 mL min^{-1}). Prior to the measurements, a correction run was performed to account for buoyancy effect with the empty crucible under the same conditions as used during analysis. These experiments allowed the thermal decomposition analysis of the samples to calculate the amount of FAS grafted in the functionalized samples (calculation in SI, Tables S1 and S2). The gases released during heating of the functionalized sample BN-FAS were analyzed with a Netzsch QMS 403 D Aëolos mass spectrometer coupled to Netzsch TG 209 F1 Libra thermal analyzer.

Micro X-ray fluorescence (μXRF) was carried out on unmodified and functionalized BN pellets to map the distribution of FAS. The samples were encased in Struers EpoFix resin and then dry-ground on 500 grit SiC paper to expose the internal surface for analysis. After grinding, the samples were cleaned by ultrasonication in acetone for 10 min and then air-dried for 15 min. An EDAX Orbis PC μXRF spectrometer equipped with a 50 kV Rh anode X-ray tube and an 80 mm^2 Si(Li) energy-dispersive detector was used to map the distribution of Si in the samples. The beam voltage, beam spot size and dwell time were set to 30 kV, 30 μm and 100 ms respectively to ensure high spatial resolution and high contrast mapping [33]. The scan format was set to 256 × 200 to achieve a pixel size of around 18.6 μm.

2.5.2. Structural features

Powder X-ray diffraction (XRD) in reflection mode was carried out using a PANalytical X'Pert Pro X-ray diffractometer with an anode voltage of 40 kV and an emission current of 20 mA using a monochromatic Cu Kα radiation (λ = 1.54178 Å). The XRD detector used was an X'Celerator silicon strip detector. We recorded 1646 points over a 2θ angle range of 5–60° with a step size of 0.033°. Powder samples were ground prior to measurement and pelletized samples were analyzed directly.

Nitrogen sorption isotherms were collected using a Micromeritics 3Flex porosity analyzer at −196 °C. All samples were first degassed ex-situ overnight at 140 °C and 0.2 mbar and then degassed in-situ at 120 °C for 4 h at 0.0030 mbar. Specific surface area was evaluated following the "BET surface identification" method (BETSI) [34], expanding on the Brunauer-Emmett-Teller (BET) theory [35]. The total pore volume for pore sizes up to 12 nm was estimated from the volume of N_2 adsorbed at a relative pressure P/P_0 of 0.99. We obtained pore size distributions in the pore width range 0.5–10 nm from the adsorption branch of the N_2 isotherms using non-local density functional theory (NLDFT) with a carbon slit-shaped pore geometry kernel. This was used to determine the micropore volume, considering pores with a width below 2 nm.

Mercury intrusion porosimetry (MIP) was carried out using a Micromeritics AutoPore IV instrument. All three pelletized samples were tested. Prior to measurements, samples were dried under vacuum at 120 °C overnight to remove any moisture. For each sample, five pellets were added to a mercury penetrometer with a capillary intrusion stem volume of 1.1 cm^3. For the low-pressure step, an evacuation pressure of 50 μmHg was applied for 5 min and mercury was then filled at a pressure of 37 mbar and left to equilibrate for 10 s. For the high-pressure measurement, a maximum pressure of 2275 bar with an equilibration time of 10 s was used. The AutoPore IV software (version 9500) was used to obtain the pore size distribution in the range 2 nm–325 μm.

The overall pore size distribution (0.5 nm–325 μm) was obtained by combining the results from both N_2 sorption isotherms at −196 °C (≈0.5 nm–10 nm), and mercury intrusion porosimetry measurements (2 nm–325 μm) [36]. To do so, we assumed continuity between both pore size distributions obtained via low pressure N_2 adsorption and MIP [37]. To select the transition point in the overlapping region of each pore size distribution, we favored pore sizes obtained via N_2 sorption over MIP. As the mercury pressure increases towards smaller pore sizes during the measurement, the results would be less accurate at higher pressures due to possible compression of the pellet.

2.6. Gas sorption testing

2.6.1. Equilibrium testing

CO_2 (99.9990%, N5.0 research grade, BOC) and N_2 (99.99990%, N6.0 grade, BOC) sorption isotherms were collected using a Micromeritics 3Flex porosity analyzer at 25 °C. All samples were first degassed ex-situ overnight at 140 °C and 0.2 mbar, and then degassed in-situ at 120 °C for 4 h at 0.0030 mbar.

CO_2 (99.9990%, N5.0 research grade, BOC) sorption isotherms were also collected using an Quantachrome Autosorb iQ3 porosity analyzer at 20, 30 and 40 °C for the kinetic study. All samples were degassed ex-situ at 50 °C for 1 h, at 100 °C for 2 h, and finally at 120 °C for 12 h at 0.0053 mbar following our previous method [36].

We note that all the isotherm data is available as supplementary information, using the Adsorption Information File (AIF) format [38]. The AIF files can be opened using the Notepad function.

2.6.2. Kinetic testing

We carried out kinetic testing to extract the kinetic rate constant in the three pellet samples BNp, BN-FASp and BNp-FAS following the method described in Azzan et al. [36] For each measurement, about 100 mg of samples was needed (~2–3 pellets). Dynamic sorption experiments were carried out at two different helium flow rates: 10 cm^3 min^{-1} and 60 cm^3 min^{-1} (99.9990%, N5.0 CP grade, BOC). The adsorbent was saturated at CO_2 partial pressures of 0.12 and 0.94 bar, and 0.11 and 0.73 bar for experiments at 10 cm^3 min^{-1} and 60 cm^3 min^{-1}, respectively. All these experiments were conducted at a total pressure of 1.01 bar. The desorption of CO_2 from each adsorbent was tracked by switching to pure helium (inert gas) flow at the aforementioned flow rates, which facilitates extraction of the kinetics through a mathematical model. To determine the temperature dependence of the adsorption kinetics, time-resolved desorption curves were obtained at three different temperatures: 33, 52 and 72 °C for BNp, and 10, 20 and 30 °C for BN-FASp and BNp-FAS. The samples were first degassed ex-situ using the procedure described in section 2.6.1 for the CO_2 and N_2 isotherm measurements. They were then degassed in-situ within the dynamic sorption cell at 100 °C for 2 h prior to the desorption experiments.

A derivative-free optimizer was used to fit mathematical models that describe the mass transport within the system to the experimental desorption curves, as described in Azzan et al. [36] Using the approach, both equilibrium and kinetic parameters can be extracted. However, in this work, the CO_2 adsorption capacity on BN-FASp and BNp-FAS was deemed to be too low, even at reduced temperatures, for the experimental desorption curves to be resolved sufficiently to accurately estimate adsorption equilibria and kinetics simultaneously. Therefore, the CO_2 volumetric adsorption isotherms (section 2.6.1) were provided as

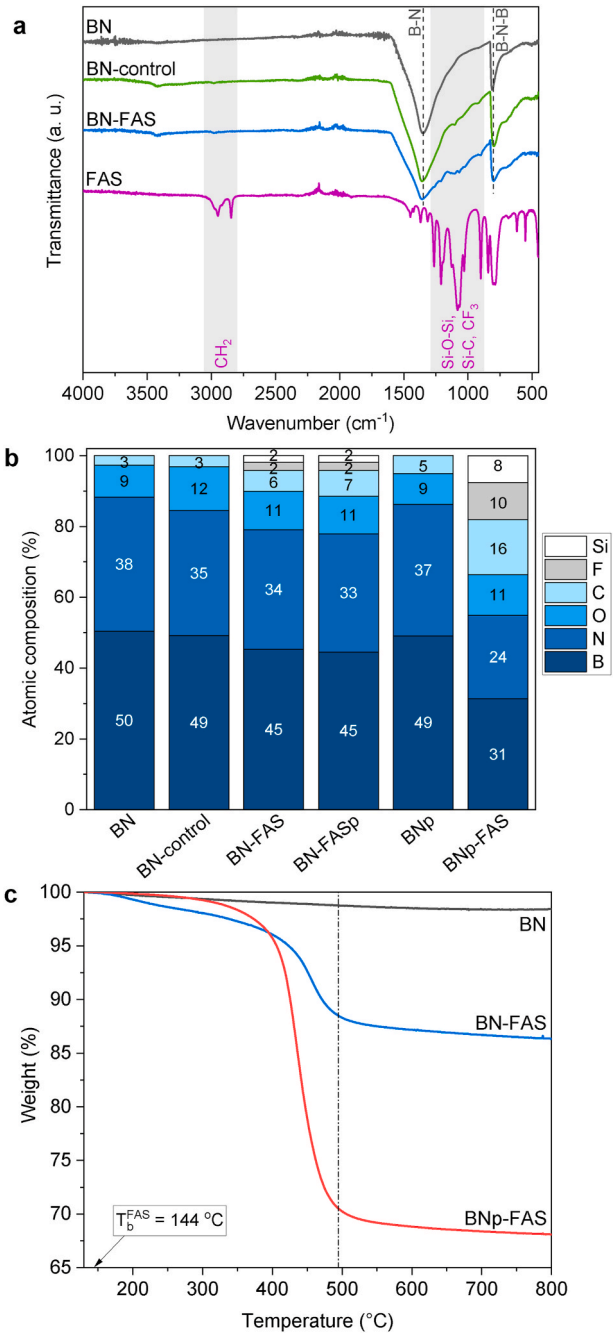

Fig. 3. Chemical analyses of unmodified and functionalized porous BN. (a) FTIR spectra for route 1 samples. (b) Atomic composition derived from XPS for routes 1 and 2 samples. (c) TG curves in air for routes 1 and 2 samples. T_b^{FAS} refers to the boiling point of trimethoxy(3,3,3-trifluoropropyl)silane (FAS), i. e., 144 °C.

an input to the mathematical model, and the kinetic parameters (k_{1,CO_2} and k_{2,CO_2}) were varied to fit the time-resolved experimental desorption curves to the mathematical model described in the previous work. The details of the validation of this approach can be found in section 10.1 of Appendix A – Supplementary data. The experimental desorption curves along with the corresponding model fits are shown in Supplementary Fig. S14. A single-site Langmuir (SSL) model was used to describe the adsorption equilibrium of CO_2 on BNp and BNp-FAS, and a dual-site Langmuir (DSL) model was used for BN-FASp. The kinetics of adsorption was modeled using a two-parameter lumped kinetic rate constant that incorporates contributions analogous to macropore and micropore

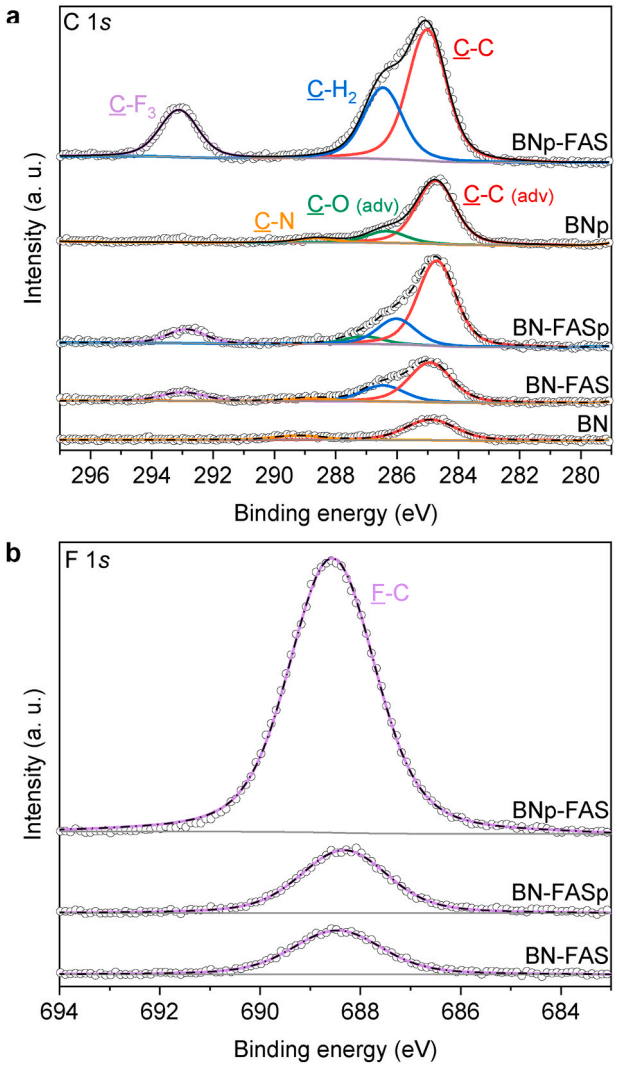

Fig. 4. High-resolution XPS and peak fitting of the (a) C 1*s* and (b) F 1*s* core levels of the unmodified and functionalized porous BN samples.

resistance within the adsorbent pellet. The equations that describe the equilibrium and kinetics of CO_2 sorption in these experiments are described in section 10.2 of Appendix A – Supplementary data.

We note that to carry out experiments at sub-ambient temperatures, the set-up described in our previous study [36] was modified as follows. A thermo-electric cooler (Laird ETX25-12-F1-6262-TA-W6, Laird Thermal Systems GmbH, Germany) along with an OEM Precision Temperature Controller (TEC-1090-HV, Meerstetter Engineering GmbH, Switzerland) was used to ensure isothermal operation between 5 and 100 °C. The ambient-side temperature of the thermo-electric cooler was maintained at 20 °C using a 6-pass liquid cold plate heat-sink (Aavid, U. S.A.). The heat-sink was supplied with water at 20 °C from a circulating chiller (Huber Minichiller 300, Huber, Germany). The adsorption cell was also rebuilt in-house to allow for good thermal contact between the cell and the thermoelectric cooler. The adsorption cell was insulated using a foam cover that is placed on the exposed surface. The modifications to the experimental set-up are shown in Fig. S13 of Appendix A – Supplementary data.

3. Results and discussion

3.1. Confirming functionalization and composition

We first confirmed functionalization for both routes 1 and 2 using

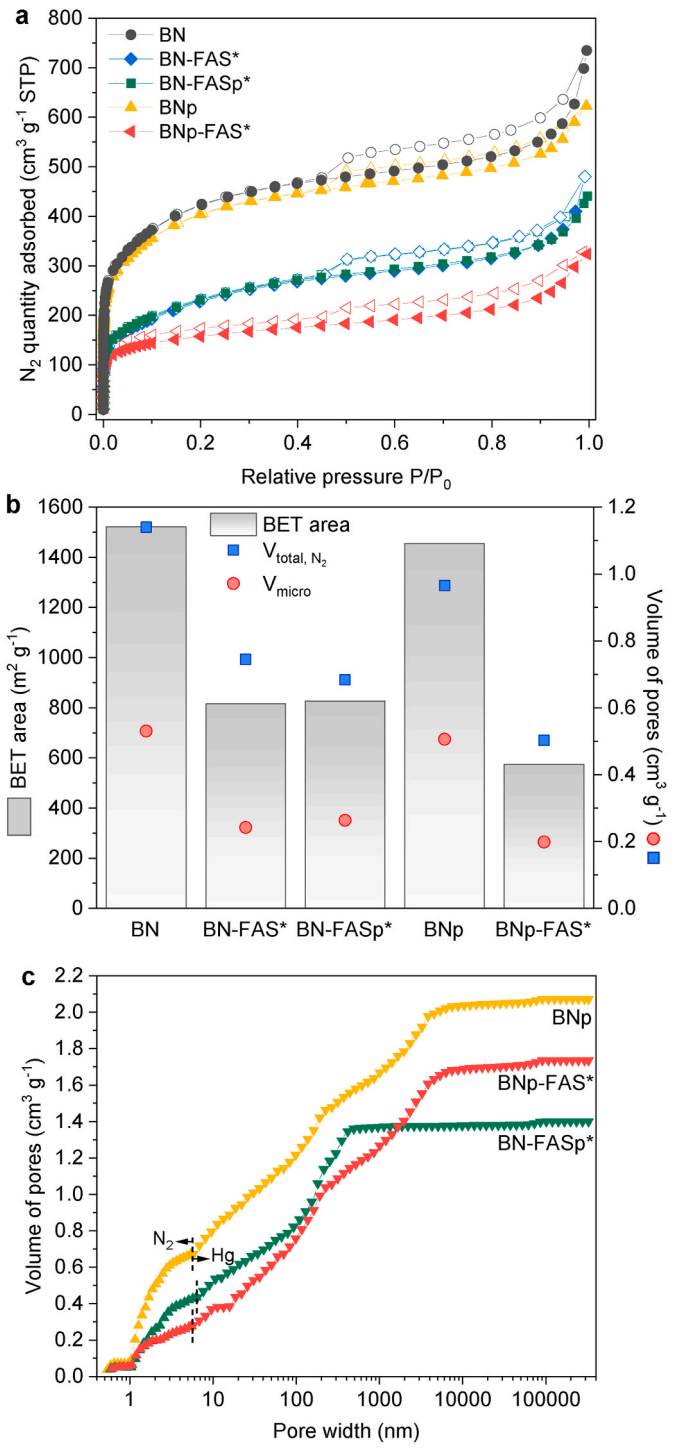

Fig. 5. Porosity analyses of unmodified and functionalized porous BN. (a) N_2 sorption isotherms at −196 °C. (b) Associated textural parameters extracted from N_2 sorption measurements. Note: total pore volumes V_{tot,N_2} correspond to pore sizes up to 12 nm as obtained from N_2 sorption. (c) Pore size distribution based on the combination of N_2 sorption at −196 °C and mercury intrusion porosimetry. Note: the dotted lines represent the cut-off points used to combine the pore size distributions obtained from N_2 sorption isotherms and MIP (see Fig. S7).

FTIR and XPS (Figs. 3 and 4). FTIR was carried out on powder samples (BN, BN-control and BN-FAS) and FAS for comparison (Fig. 3a; zoomed-in spectrum in Fig. S3a). Results showed B–N and B–N–B bands at 1353 cm^{-1} and 801 cm^{-1} respectively, in all powder samples [39]. We observed in the BN-control sample a band at 1104 cm^{-1} indicating the presence of B–O bonds, likely due to partial degradation of porous BN during the washing step with ethanol. This was confirmed by a higher O content than in porous BN in the atomic composition derived from XPS (Fig. 3b). Looking at BN-FAS, we observed new bands in the region 1290–865 cm^{-1}. These bands corresponded to Si–*O*–Si, Si–C and $–CF_3$ observed in FAS [39]. Bands in the region 3065–2793 cm^{-1} corresponded to the $–CH_2$ groups in FAS [39]. These bands showed low intensity in BN-FAS, potentially due to the low content of FAS, which will be discussed later in this section. XPS analyses for C 1*s* and F 1*s* showed C–F and C–H peaks corresponding to FAS in all functionalized samples (Fig. 4), whereas only noise was observed in the F 1*s* spectrum of unmodified BN (Fig. S4). We should note that the C–C peaks can be attributed to both adventitious carbon (also observed in BN and BNp) and FAS. The estimated atomic composition confirmed that pelletization did not significantly impact the chemistry of the samples when comparing BN vs. BNp, and BN-FAS vs. BN-FASp (Fig. 3b and S1). We noted that the contents of Si and F were higher in BNp-FAS (route 2) compared to BN-FASp (route 1). This may be partly due to XPS being a surface-sensitive technique, and FAS is expected to be mainly present at the surface of BNp-FAS pellets after the CVD treatment (Fig. 1b).

We used TGA and TG-MS to further confirm functionalization qualitatively and quantitatively. The sharp weight loss observed in TGA between 350 and 495 °C in BN-FAS and BNp-FAS, but not in BN, corresponded to the removal of FAS molecules or fragments. In TG-MS, we observed that H_2O and CH_3OH were the main species decomposing up to 350 °C in BN-FAS (Fig. S3c), implying that non-grafted CH_3O^- groups from FAS were removed (Fig. S6) [40]. Between 350 and 800 °C, CF_2 and CF_3 signals showed that the alkyl chains $F_3C\text{-}(CH_2)_2$ were removed (Fig. S3c) [40]. As the boiling point of FAS is 144 °C, these results show that FAS was strongly attached to porous BN, i.e., via covalent bonding (Fig. S6). The bonds are most likely formed with the OH groups present in porous BN as per equation (2) [41], with R representing the BN structure with hydrophilic OH groups, and R' the hydrophobic alkyl chain of FAS:

$$R-OH_{(s/l)} + (CH_3O)_3 - Si - R'_{(l)} \rightleftharpoons R-O-Si(OCH_3)_2R'_{(s/l)} + CH_3OH_{(l)} \quad (2)$$

The estimated content of FAS grafted in each functionalized sample was: 18.4 wt% in BN-FAS and BN-FASp (1.13 mmol per g of BN) and 49.3 wt% in BNp-FAS (3.11 mmol per g of BN). Details of the calculations can be found in Appendix A – Supplementary data (Tables S1 and S2). A possible hypothesis explaining the different loadings between both routes is that FAS molecules could react with each other during the silylation process, without grafting to porous BN. Therefore, these molecules would be removed during the filtration of the functionalized BN powder. In the rest of this study, we have used the calculated FAS concentrations to report gas sorption results (i.e., N_2, CO_2 and H_2O in this study) per gram of porous BN (as opposed to per gram of sample). These results are indicated with an asterisk "*" after the corresponding samples names.

3.2. *Assessing pore structure and porosity*

We used N_2 sorption at −196 °C to survey the impact of functionalization on BET area and porosity (Fig. 5a and b). Relevant results are expressed after weight adjustment (annotated with "*"). BNp and porous BN powder had similar BET areas (1455 $m^2\ g^{-1}$ and 1521 $m^2\ g^{-1}$ respectively), as well as BN-FASp* and BN-FAS* but with lower values (827 $m^2\ g^{-1}$ and 816 $m^2\ g^{-1}$ respectively). We attribute the decrease in BET area and porosity to the synthesis process employed for route 1, i.e., use of toluene and/or ethanol, as opposed to the silylation reaction itself. This interpretation arises from the study of the BN-control sample (Fig. S5). After route 2, BNp-FAS* had a BET area of 575 $m^2\ g^{-1}$, which may indicate pore blockage.

We combined pore size distributions from N_2 sorption analyses at

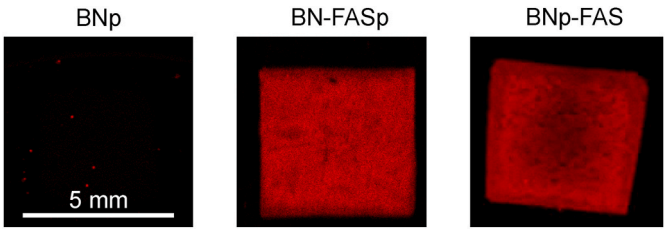

Fig. 6. Pelltet cross-section showing silicon elemental mapping (in red) using μXRF for BNp, BN-FASp and BNp-FAS. White line corresponds to 5 mm and all three images are at the same scale.

−196 °C and mercury intrusion porosimetry (Fig. S7) to obtain the overall pore size distribution over the range 0.5 nm–325 μm (Fig. 5c) [37]. As expected, the total volumes of pores in Fig. 5b and c differ. As MIP can survey larger pores than N_2 sorption at −196 °C (Fig. S7), both techniques are required to get an accurate indication of the total pore volume in samples that have a very wide pore size distribution (i.e., also containing meso- and macropores). The volumes of micropores (<2 nm) are identical in both Fig. 5b and c as only the contribution from N_2 sorption is considered for this size range.

BNp exhibited micropores, mesopores and macropores. BNp-FAS obtained via CVD showed a similar profile, but with lower pore volume at every scale, particularly in the region of pores smaller than 100 nm. This observation suggests that FAS blocked these smaller pores. BN-FASp had a distinct profile with hardly any pores larger than 465 nm but a significant amount of small pores.

μXRF shed light on the location of FAS molecules in the functionalized samples (Fig. 6). We performed cross-sectional mapping of silicon in BNp as a control. In both functionalized pellets, Si atoms can be clearly observed. BN-FASp displayed a uniform distribution of Si apart from the top and bottom surfaces of the pellet, which appeared slightly less concentrated. This could be due to the pelletization process, leading to non-uniform structure between the surface and the bulk. In BNp-FAS, the distribution of Si was even less uniform, as expected due to the CVD process. A less concentrated amount of Si appears at the centre of the pellet. This is likely related to the diffusion process of FAS during which molecules may not have reached the centre of the pellet. We excluded any impact from the grinding process during sample preparation, as the μXRF instrument performs auto-focusing on each point to ensure that the sample surface is in plane before analysis. The μXRF images support the MIP analyses (Fig. 5c): the higher proportion of large pores for BNp-FAS as opposed to BN-FASp could point to a deeper diffusion of FAS molecules inside the BNp-FAS pellet.

3.3. Probing the hydrophobicity

We measured water contact angles to quickly probe hydrophobicity of the pellets. Both BNp and BN-FASp absorbed water within 1–2 s of deposition, which made the recording of contact angles inaccurate (Supplementary Fig. S8 and videos). Corresponding contact angles would be smaller than 90°, indicating hydrophilic surfaces. On the contrary, BNp-FAS displayed a static contact angle of 133.2°, corresponding to a hydrophobic surface. Hydrophobic contact angles can depend on the chemistry of the samples but also on their surface roughness, which may have an impact here since sample surfaces underwent various treatments with pelletization and CVD steps (Fig. 2). Therefore, it was difficult to draw definite conclusions from water contact angle measurements and we proceeded with complementary analyses.

We carried out water sorption isotherms at 22 °C to probe the behavior of pelletized samples upon water vapor exposure (Fig. 7a). We observed for BNp a step around $P/P_0 = 0.25$ indicating condensation and/or degradation of porous BN at this humidity level. Therefore, we repeated the measurements on fresh samples and stopped the measurement at this humidity level to compare the stability of our pellets (Fig. 7b). We observed a large gap between desorption and adsorption in BNp, indicating that the structure of porous BN was damaged, and its chemistry would have changed upon prolonged moisture exposure. These chemical and structural changes will be discussed in greater detail in sections 3.4 and 3.5. In the case of BN-FASp, a significant amount of water was adsorbed, confirming the contact angle analysis. Interestingly, this sample adsorbed more water than BNp per gram of boron nitride after weight adjustment. At this time, we cannot provide a verified explanation for this behavior. However, we speculate that since these sorption experiments are long, the structure of the sample may change during the analysis if it is not fully water stable. This change might lead to an increased water sorption. Finally, BNp-FAS adsorbed less water than BNp and BN-FASp up to a relative pressure of 0.6, suggesting improved hydrophobicity thanks to the silane protection, and supporting the previous contact angle findings. We note that BNp-FAS has lower BET area than BNp and BN-FASp (Fig. 5a), which could potentially translate to lower water adsorption. However, we should note that although N_2 molecules may not be able to access partially blocked pores at – 196 °C, water molecules could still do so. In summary, water sorption isotherms have provided an insight into the hydrophobicity of our materials, but this needs further investigation as shown in the following section.

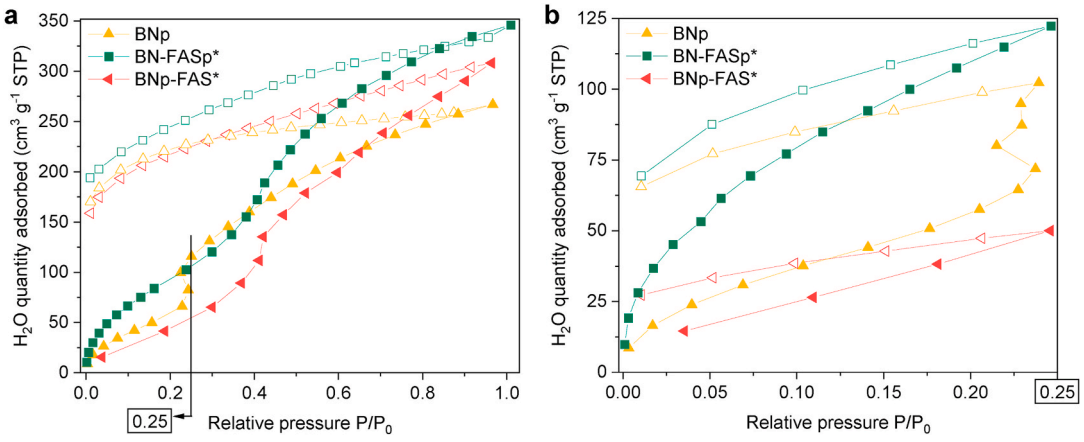

Fig. 7. Water vapor sorption isotherms at 22 °C for BNp, BN-FASp and BNp-FAS: (a) Up to 1 bar; (b) Up to $P/P_0 = 0.25$. The black arrow in (a) indicates where the second measurement, in (b), was stopped.

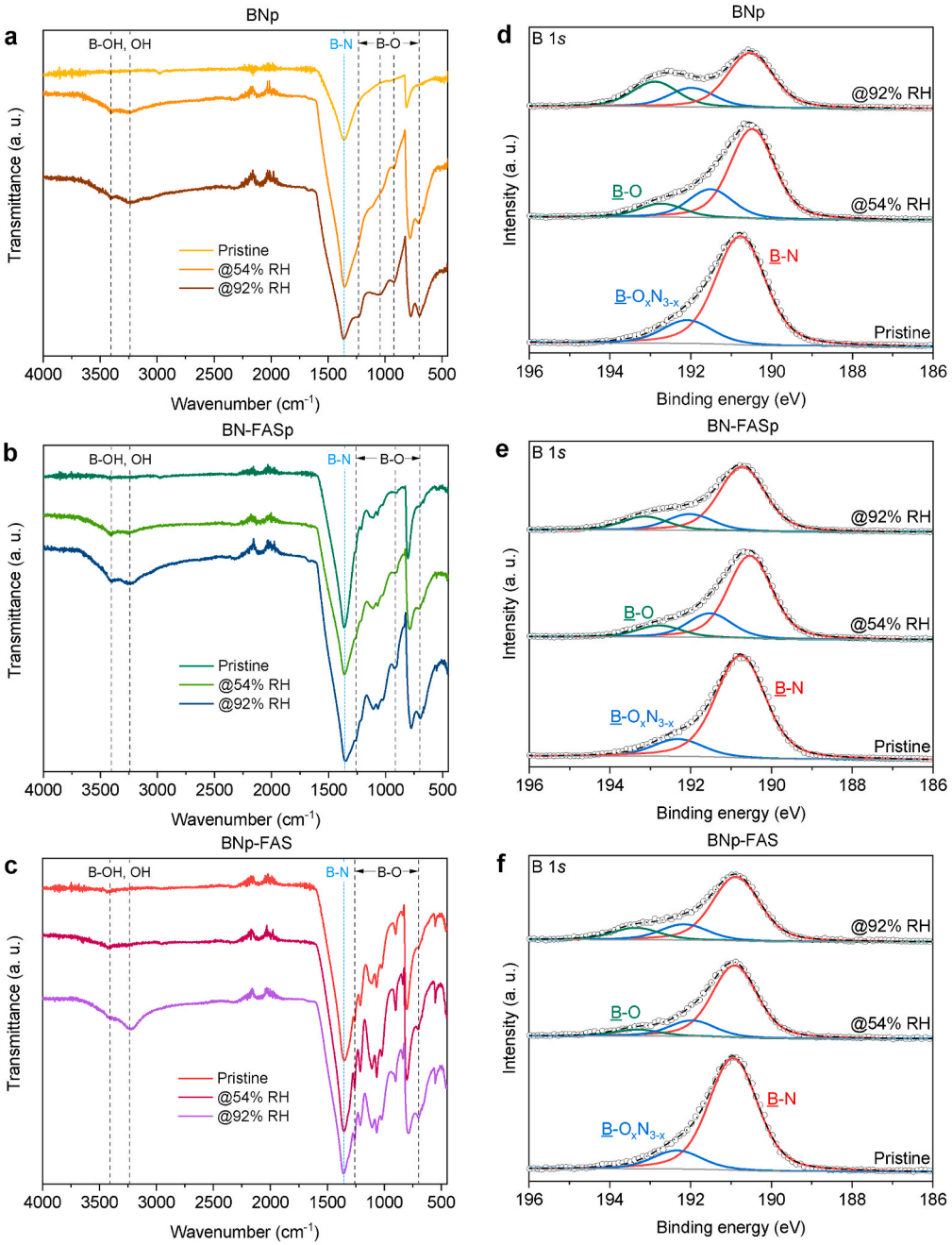

Fig. 8. FTIR spectra before and after humidity testing for: (a) BNp; (b) BN-FASp; (c) BNp-FAS. High-resolution XPS and peak fitting of the B 1*s* core level before and after humidity testing for: (d) BNp; (e) BN-FASp; (f) BNp-FAS.

3.4. Assessing the moisture impact on chemistry

To probe the impact of moisture on the chemistry of the unmodified and functionalized pelletized samples, we used FTIR and XPS prior to and after moisture exposure at 54% and 92% RH for 24 h (Fig. 8). All samples exhibited B–O bonds after exposure to moisture, which was even more pronounced at 92% RH (Fig. 8a–c), indicating partial degradation of the BN-based materials. The B–N bands at 1355 and 776 cm^{-1} were still visible after moisture exposure, meaning some BN had been preserved. XPS analyses for B 1*s* confirmed the FTIR results with appearance of B–O chemical environments in all samples (Fig. 8d–f). B 1*s* XPS peaks corresponding to B–N bands were still predominant in the functionalized pellets compared to unmodified BNp, confirming that BN was still present despite water exposure.

To get a better quantification of the moisture impact and the stability of the samples, we estimated the atomic composition based on XPS results (Fig. S9a). We then calculated the B–N/B–O ratios, since porous BN reacts with water and degrades into boron oxide via the release of ammonia, leading to a decrease in N atoms after moisture exposure [14]. We obtained B–N/B–O ratios of 6.7 in BNp, 7.2 in BN-FASp and 11.2 in

Table 1
Ratios of B–N/B–O bonds (excluding B–*O*–N) derived from XPS after moisture exposure at 54% RH and 92% RH.

Sample	After 54% RH	After 92% RH
BNp	6.7	2.2
BN-FASp	7.2	4.8
BNp-FAS	11.2	5.4

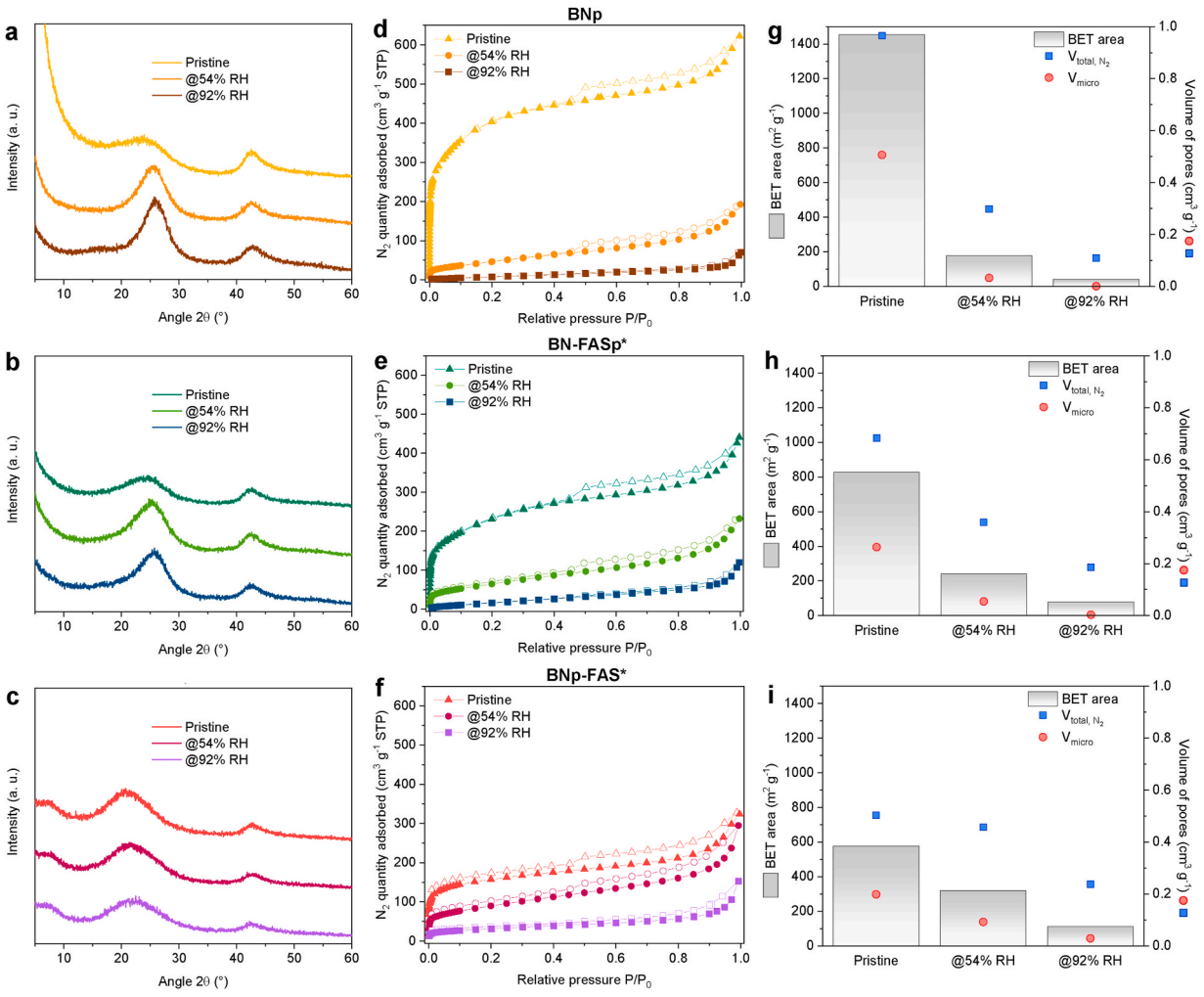

Fig. 9. XRD patterns before and after humidity exposure for: (a) BNp; (b) BN-FASp*; (c) BNp-FAS*. N_2 sorption isotherms at −196 °C before and after humidity exposure for: (d) BNp; (e) BN-FASp*; (f) BNp-FAS*. Textural parameters obtained from N_2 sorption isotherms before and after humidity exposure for: (g) BNp; (h) BN-FASp*; (i) BNp-FAS*. Note: total pore volumes V_{tot,N_2} correspond to pore sizes up to 12 nm as obtained from N_2 sorption.

BNp-FAS after exposure to 54% RH (Table 1). These ratios decreased after exposure to 92% RH, reaching 2.2 in BNp, 4.8 in BN-FASp and 5.4 in BNp-FAS. This implied that more significant degradation took place in unmodified BNp compared to the functionalized pellets, corresponding to better protection of the chemistry of BN thanks to functionalization. The Si 2*s* spectra did not show shifts in binding energy upon moisture exposure (Figs. S9b and S9c), suggesting that the siloxane network at the surface of porous BN was not impacted. Corroborating the contact angle measurements and the water sorption analyses, XPS data pointed to the better moisture stability of BNp-FAS compared to BN-FASp.

3.5. *Assessing the moisture impact on structure and porosity*

To probe the impact of moisture on the structure of the unmodified and functionalized pelletized samples, we used XRD prior to and after moisture exposure at 54% and 92% RH for 24 h (Fig. 9a–c). Results for powder samples can be found in SI (Fig. S10). Prior to moisture exposure, unmodified BNp exhibited two broad humps around 24° and 44° (Fig. 9a), which typically correspond to the (002) and (100) planes in graphitic-like structures, such as crystalline hexagonal BN [3,42]. These two features appeared narrower and more defined after moisture exposure at 54% RH, and even narrower after 92% RH. This implies that the structure of BNp became more crystalline overall upon moisture exposure due to the reaction with water. We hypothesize that water primarily reacts with the amorphous phases in porous BN and decomposes them, while leaving more crystalline phases in the samples intact, therefore exhibiting higher crystallinity on average after moisture exposure [14]. In BN-FASp, we observed a similar effect after moisture exposure with more defined peaks, but with no significant difference between 54% and 92% RH exposure. On the contrary, the signals were still very broad in BNp-FAS, implying that the sample remained highly amorphous. These observations align with the XPS analyses presented above.

We probed the impact of moisture on the porosity of the samples via N_2 sorption isotherms and the derivation of textural parameters (Fig. 9d–i). When looking at unmodified BNp, we observed that exposure at 54% and 92% RH dramatically reduced BET area and porosity (Fig. 9d and g). BET area decreased from 1455 $m^2\ g^{-1}$ to 177 $m^2\ g^{-1}$ after 54% RH exposure (87% reduction), and to 40 $m^2\ g^{-1}$ after 92% RH exposure (99% reduction). In comparison, BN-FASp* had its BET area decrease from 827 $m^2\ g^{-1}$ to 239 $m^2\ g^{-1}$ after 54% RH exposure (71% reduction), and to 78 $m^2\ g^{-1}$ after 92% RH exposure (91% reduction) (Fig. 9e and h). Finally, BNp-FAS* had its BET area decrease from 575 $m^2\ g^{-1}$ to 319 $m^2\ g^{-1}$ after 54% RH exposure (45% reduction), and to 112 $m^2\ g^{-1}$ after 92% RH exposure (81% reduction) (Fig. 9f and i). Accessible BET area remained after exposure at 92% RH in the functionalized pellets BN-FASp and particularly BNp-FAS, whereas unmodified BN hardly had any porosity left. Another interesting observation is the apparent advantage of pelletization after high humidity exposure, as observed by the higher BET area in BNp and BN-FASp*, compared to BN

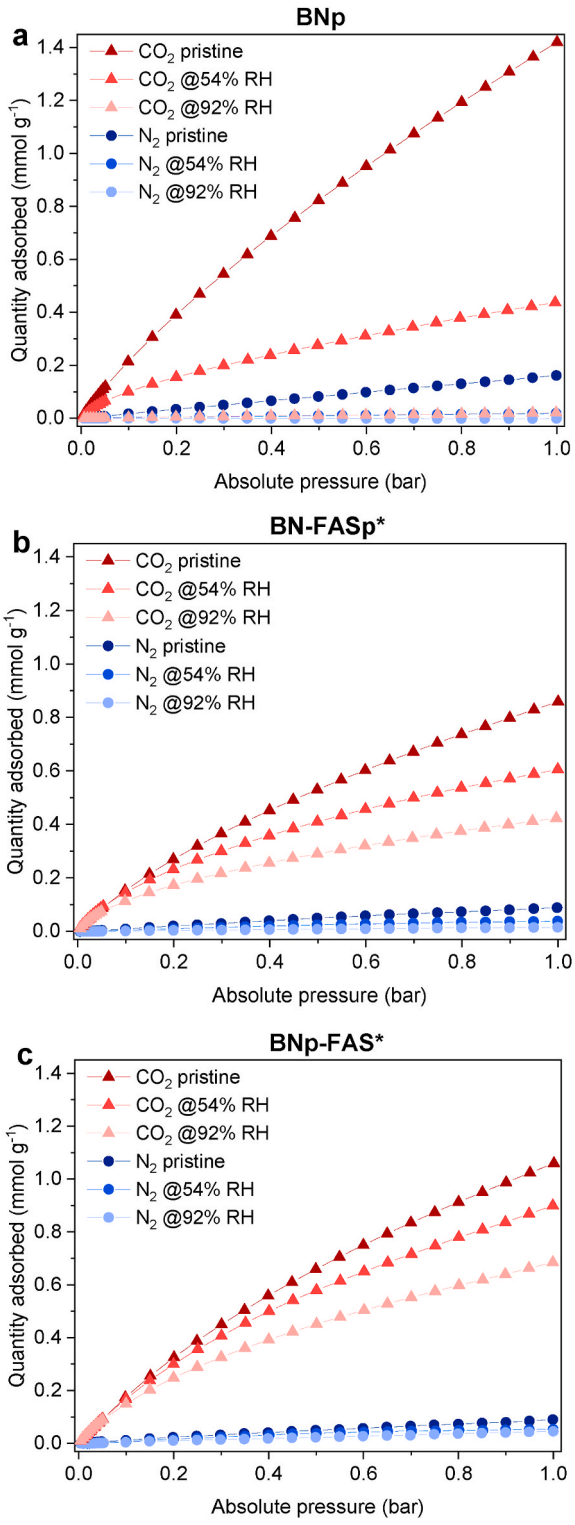

Fig. 10. CO_2 and N_2 sorption isotherms at 25 °C before and after moisture exposure at 54% and 92% RH for: (a) BNp; (b) BN-FASp*; (c) BNp-FAS* (* indicates that quantities adsorbed were adjusted per g of BN; see section 3.1).

and BN-FAS respectively (Fig. S10f).

3.6. Probing equilibrium separation properties

To understand the practical efficiency of our functionalization methods and progress towards scale-up, we measured CO_2 and N_2 sorption isotherms at 25 °C on the three pellets for all three scenarios: pristine, after 54% RH moisture exposure and after 92% RH moisture exposure (Fig. 10). In the case of BNp, CO_2 adsorption capacity significantly decreased after moisture exposure at 54% RH, and further at 92% RH where hardly any CO_2 adsorbed over the pressure range surveyed (Fig. 10a). N_2 adsorption capacity at 25 °C also decreased after water exposure. These results were expected based on the previous porosity analyses (Fig. 9d and g). Looking at both BN-FASp and BNp-FAS, CO_2 adsorption capacity slightly decreased after moisture exposure but was less impacted compared to BNp (Fig. 10b and c). We note that we also measured the CO_2 and N_2 sorption isotherms at 20, 30 and 40 °C for all three samples in dry conditions (Fig. S11).

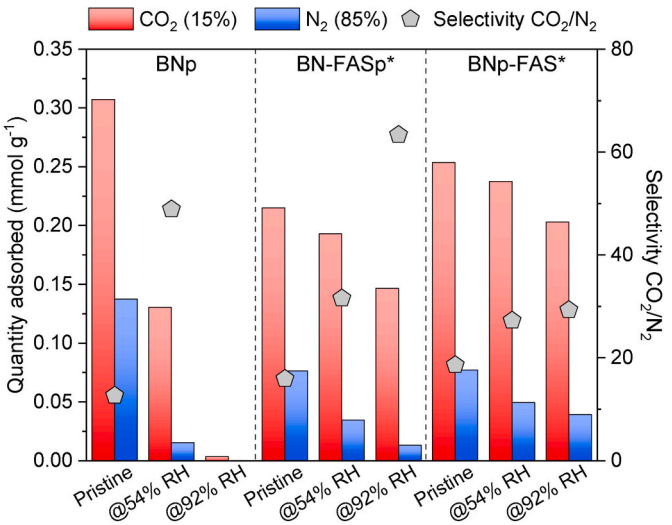

Fig. 11. CO_2 and N_2 uptakes at 25 °C for a composition of $CO_2/N_2 = 0.15{:}0.85$ before and after moisture exposure, and associated selectivity values (not defined for BNp @92% RH due to low value for N_2 adsorption).

To estimate the CO_2/N_2 selectivity, we extracted the capacities at given pressures corresponding to a common composition in post-combustion carbon capture scenarios: $CO_2/N_2 = 0.15/0.85$ (Fig. 11). We then calculated the pure component selectivity using equation (3), with q_{CO2} and q_{N2} being the CO_2 capacity at 0.15 partial pressure and the N_2 capacity 0.85 partial pressure, respectively:

$$S = \frac{q_{CO2}}{q_{N2}} \frac{0.85}{0.15} \tag{3}$$

We report the capacity values and the calculated selectivities for all pellets in Fig. 11. The selectivity for BNp after moisture exposure at 92% RH was not determined due to the extremely low N_2 capacity. In summary, prior to moisture exposure, functionalization very slightly enhances selectivity while maintaining reasonable uptake for both BN-FASp and BNp-FAS compared to unmodified BNp. After exposure to high RH, functionalization helps maintain a reasonable balance between selectivity and uptake, which can be desirable for industrial applications. Exposure to moisture enhances selectivity owing to the marked decrease in N_2 uptake caused by the loss in porosity.

3.7. Estimating kinetics of adsorption

The experimental CO_2 adsorption isotherms obtained using the methodology described in section 2.6.1 and in Azzan et al. [36], along with the fitted isotherm models, are shown in Fig. 12a–c. The lumped kinetic constants for CO_2 (k_{CO_2}) obtained by carrying out dynamic sorption tests are shown in Fig. 12d–f. The equations that describe the equilibrium and kinetics of CO_2 sorption in these experiments are described in S10.1 of Appendix A –Supplementary data, and the resulting model parameters are shown in Table 2. The kinetic model

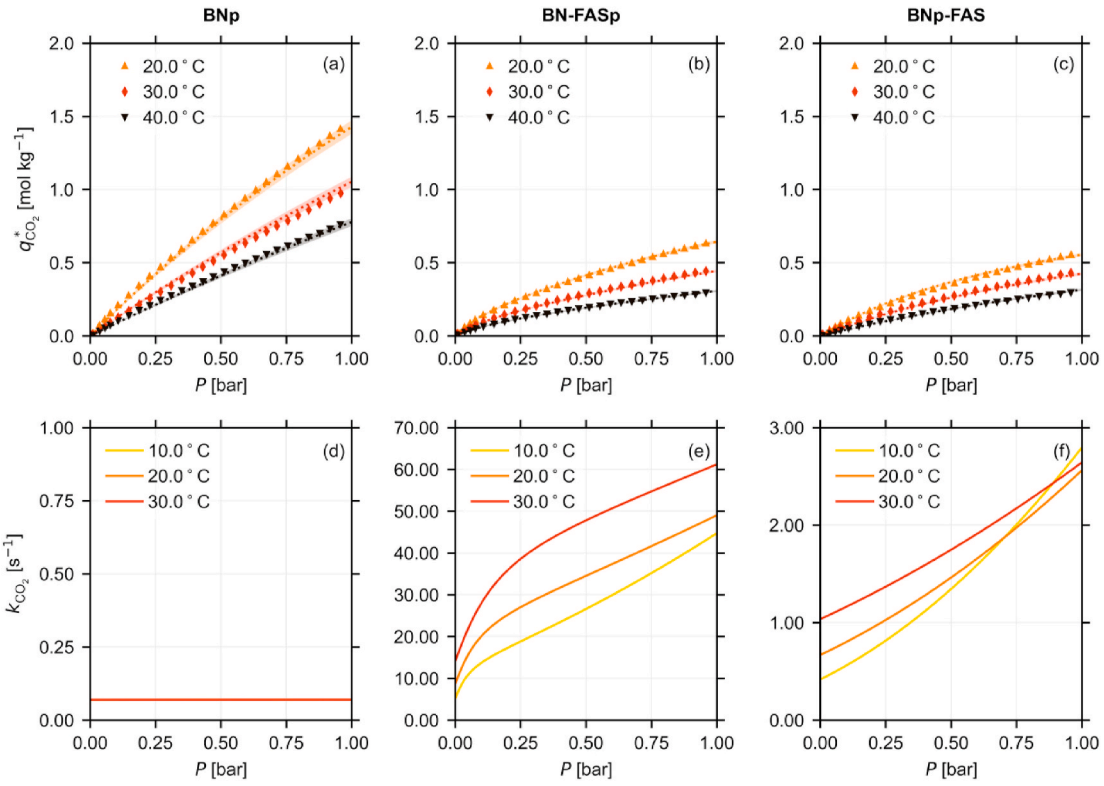

Fig. 12. CO_2 sorption isotherms $q^*_{CO_2}(P,T)$ at 20, 30 and 40 °C for: (a) BNp; (b) BN-FASp; (c) BNp-FAS. Isotherm model fits for: (d) BNp (single-site Langmuir model); (e) BN-FASp (dual-site Langmuir model); (f) BNp-FAS (single-site Langmuir model). The shaded region corresponds to the 95% confidence bounds for the model fits with respect to the experimental data (note: the shaded region is very narrow). Corresponding lumped kinetic rate constant k_{CO_2} for: BNp (d), BN-FASp (e) and BNp-FAS (f). Note: for BNp, k_{CO_2} was obtained using experiments carried out at 33, 52 and 72 °C as described in Ref. [36].

Table 2
Parameters for the CO_2 equilibrium isotherms obtained from fitting the relevant isotherm model to the data from Fig. 12, and the corresponding parameters for the CO_2 adsorption kinetics for BNp, BN-FASp and BNp-FAS (more information on the equations and parameters in section 10.1 of Appendix A – Supplementary data). For perspective, kinetics parameters for CO_2 sorption in zeolite 13X measured using the same technique as the one used here are reported in the table too (taken from Ref. [36]).

Parameters	Unit	BNp	BN-FASp	BNp-FAS	Zeolite 13X pellet
Isotherm parameters					
q_{sb,CO_2}	mol kg^{-1}	7.01 ± 0.09	1.74 ± 0.31	1.13 ± 0.17	
b_{0,CO_2}	($\times 10^{-7}$) m^3 mol^{-1}	2.30 ± 0.03	5.61 × 10^{-3} ± 9.59 × 10^{-4}	0.39 ± 0.06	
$-\Delta U_{b,CO_2}$	kJ mol^{-1}	24.87 ± 0.04	41.00 ± 0.08	32.40 ± 0.08	
q_{sd,CO_2}	mol kg^{-1}	–	0.09 ± 0.03	–	
d_{0,CO_2}	($\times 10^{-7}$) m^3 mol^{-1}	–	2.94 ± 0.56	–	
$-\Delta U_{d,CO_2}$	kJ mol^{-1}	–	34.30 ± 0.501	–	
Kinetic parameters					
k_{1,CO_2}	s^{-1}	0.07 ± 0.00	920.00 ± 117.00	867.00 ± 118.00	779.18 ± 49.36 [36]
k_{2,CO_2}	s^{-1}	831.77 ± 69.51	631.00 ± 105.00	40.80 ± 4.68	75.34 ± 4.22 [36]

used in the parameter estimation for the dynamic sorption experiments can be used to infer dominant resistances to mass transfer, namely, resistance in the micropores and resistance in the macropores of the adsorbent [43]. In the case of BNp, the dominant resistance to mass transfer is in the micropores, as inferred from experimental observations reported previously. This results in a constant value for the lumped kinetic rate constant k_{CO_2} over the entire range of pressures and temperatures [36]. As for the functionalized BN samples, the parameter estimation on the dynamic sorption experiments results in much higher values of the kinetic rate constant k, indicating a faster mass transfer. Looking at the magnitudes of the two contributions k_1 and k_2, which are analogous to resistances in micropores and macropores, respectively, we can conclude that there is negligible resistance to mass transfer in both the macro- and micropores for the case of BN-FASp. However, for BNp-FAS, although k_1 is large, k_2 is significantly smaller compared to both BNp and BN-FASp. From this, we can infer that there is a greater resistance to mass transfer in the macropores for the case of BNp-FAS, when compared to BNp and BN-FASp. BNp-FAS has a notably higher bulk density (770.5 kg m^{-3} as derived from MIP measurement) compared to BNp and BN-FASp (413.2 kg m^{-3} and 448.7 kg m^{-3}, respectively), which indicates that the functionalization has caused changes in the porosity of the pellets, leading to changes in the mass transfer process. As seen in Fig. 5c, BNp has a greater proportion of smaller micropores than for the functionalized samples, which might explain the enhanced micropore resistance for this sample.

4. Conclusions

We explored ways of enhancing the hydrolytic stability of porous BN via surface functionalization using a fluoroalkylsilane, i.e., trimethoxy (3,3,3-trifluoropropyl)silane. We trialed two functionalization methods: i) silylation of porous BN powder followed by pelletization (route 1); ii) chemical vapor deposition of alkylsilane on pre-formed porous BN pellets (route 2). These two routes led to shaped adsorbents with distinct chemical and textural features. This in turn caused changes in their hydrophobic/hydrophilic nature, as well as sorption equilibrium

and kinetic properties.

By capping the OH groups present at the surface of porous BN, the silylation partially protected the chemistry and structure of porous BN against moisture attack compared to pristine porous BN. More specifically, route 2 led to a higher silane grafting yield and produced a hydrophobic sample more structurally resistant to moisture compared to the sample obtained via route 1. This enhanced feature can be linked to the overall higher silane content in this sample and/or the greater silane concentration on the surface of the pellets.

From an equilibrium sorption point of view, for both routes, functionalization very slightly enhanced selectivity towards CO_2 in CO_2/N_2 separation while maintaining reasonable CO_2 and N_2 uptakes. Upon exposure to moisture, the gas uptakes of all the samples decreased, but significantly less for the functionalized samples owing to their greater structural stability.

Finally, sorption kinetics analyses point to different mass transfer mechanisms for the three samples, i.e., pristine porous BN and the two functionalized samples. These findings highlight the critical aspect of formulation to control dynamic sorption processes. Overall, our findings pave the way for a better understanding of the hydrolytic instability of porous BN, and for the development of further methods to functionalize porous BN to tailor its hydrophobicity.

CRediT authorship contribution statement

Anouk L'Hermitte: Writing – review & editing, Writing – original draft, Visualization, Software, Methodology, Investigation, Formal analysis, Data curation, Conceptualization. **Hassan Azzan:** Writing – review & editingWriting – review & editing, Writing – original draft, Visualization, Software, Methodology, Investigation, Formal analysis, Data curation. **Marcus H.N. Yio:** Writing – review & editingWriting – review & editing, Methodology, Formal analysis, Data curation. **Ashwin Kumar Rajagopalan:** Writing – review & editingWriting – review & editing, Software, Methodology, Formal analysis. **David Danaci:** Writing – review & editingWriting – review & editing, Methodology, Conceptualization. **Takuya Hirosawa:** Writing – review & editing, Methodology. **Toshihiro Isobe:** Writing – review & editingWriting – review & editing, Resources, Project administration. **Camille Petit:** Writing – review & editingWriting – review & editing, Validation, Supervision, Resources, Project administration, Investigation, Funding acquisition, Conceptualization.

Declaration of competing interest

The authors declare that they have no known competing financial interests or personal relationships that could have appeared to influence the work reported in this paper.

Data availability

Data will be made available on request.

Acknowledgments

ALH and CP thank Patricia Carry and Kaho Cheung for the use and support of the Analytical Laboratory in the Department of Chemical Engineering at Imperial College London, and Gwilherm Kerherve for the use and support of the XPS suite in the Department of Materials at Imperial College London. ALH and CP would also like to thank Leslie Bolton, Mark Sankey, Mandar Thakare, Sheetal Handa and Aldo Guiducci for the technical support with the bp-International Centre for Advanced Materials (bp-ICAM). ALH and CP acknowledge the funding from bp-ICAM and the funding from the Engineering and Physical Sciences Research Council (EPSRC) through the CDT in Advanced Characterization of Materials [grant 2018 NPIF EP/S515085/1]. HA acknowledges funding through a donation to the Department of Chemical Engineering, Imperial College London, by Mr. Mark Richardson. MY would like to acknowledge support from EPSRC funding [grant EP/R010161/1] and from the UKCRIC Coordination Node, EPSRC [grant EP/R017727/1]. DD would like to acknowledge funding from Research Councils UK (RCUK) [grants EP/P026214/1 and EP/T033940/1].

Appendix A. Supplementary data

Supplementary data to this article can be found online at https://doi.org/10.1016/j.micromeso.2023.112478.

References

[1] J.F. Janik, W.C. Ackerman, R.T. Paine, D.-W. Hua, A. Maskara, D.M. Smith, Boron nitride as a selective gas adsorbent, Langmuir 10 (1994) 514–518.
[2] S. Marchesini, C.M. McGilvery, J. Bailey, C. Petit, Template-free synthesis of highly porous boron nitride: insights into pore network design and impact on gas sorption, ACS Nano 11 (2017) 10003–10011.
[3] S. Marchesini, A. Regoutz, D. Payne, C. Petit, Tunable porous boron nitride: investigating its formation and its application for gas adsorption, Microporous Mesoporous Mater. 243 (2017) 154–163.
[4] F. Xiao, Z. Chen, G. Casillas, C. Richardson, H. Li, Z. Huang, Controllable synthesis of few-layered and hierarchically porous boron nitride nanosheets, Chem. Commun. 52 (2016) 3911–3914.
[5] D. Saha, G. Orkoulas, S. Yohannan, H.C. Ho, E. Cakmak, J. Chen, S. Ozcan, Nanoporous boron nitride as exceptionally thermally stable adsorbent: role in efficient separation of light hydrocarbons, ACS Appl. Mater. Interfaces 9 (2017) 14506–14517.
[6] J. Li, J. Lin, X. Xu, X. Zhang, Y. Xue, J. Mi, Z. Mo, Y. Fan, L. Hu, X. Yang, J. Zhang, F. Meng, S. Yuan, C. Tang, Porous boron nitride with a high surface area: hydrogen storage and water treatment, Nanotechnology 24 (2013), 155603.
[7] M. Maleki, A. Beitollahi, M. Shokouhimehr, Simple synthesis of two-dimensional micro/mesoporous boron nitride, Eur. J. Inorg. Chem. (2015) 2478–2485, 2015.
[8] W. Lei, D. Portehault, D. Liu, S. Qin, Y. Chen, Porous boron nitride nanosheets for effective water cleaning, Nat. Commun. 4 (2013) 1777.
[9] S. Marchesini, X. Wang, C. Petit, Porous boron nitride materials: influence of structure, chemistry and stability on the adsorption of organics, Front. Chem. 7 (2019) 160.
[10] S. Motojima, Y. Tamura, K. Sugiyama, Low temperature deposition of hexagonal BN films by chemical vapour deposition, Thin Solid Films 88 (1982) 269–274.
[11] T. Matsuda, Stability to moisture for chemically vapour-deposited boron nitride, J. Mater. Sci. 24 (1989) 2353–2357.
[12] C.G. Cofer, J. Economy, Oxidative and hydrolytic stability of boron nitride — a new approach to improving the oxidation resistance of carbonaceous structures, Carbon 33 (1995) 389–395.
[13] M. Florent, T.J. Bandosz, Irreversible water mediated transformation of BCN from a 3D highly porous form to its nonporous hydrolyzed counterpart, J. Mater. Chem. 6 (2018) 3510–3521.
[14] R. Shankar, S. Marchesini, C. Petit, Enhanced hydrolytic stability of porous boron nitride via the control of crystallinity, porosity, and chemical composition, J. Phys. Chem. C 123 (2019) 4282–4290.
[15] J. Hojak, T. Jähnichen, C. Bläker, C. Pasel, V. Mauer, L. Rasmussen, R. Denecke, D. Enke, D. Bathen, Mesoporous boron nitride in contact with water - chemical stability and adsorption properties, Results Mater. 16 (2022).
[16] I. Itskou, A. L'Hermitte, S. Marchesini, T. Tian, C. Petit, How to tailor porous boron nitride properties for applications in interfacial processes, Acc. Mater. Res. (2023), https://doi.org/10.1021/accountsmr.2c00148.
[17] R.M. Ravenelle, F. Schubler, A. D'Amico, N. Danilina, J.A. van Bokhoven, J. A. Lercher, C.W. Jones, C. Sievers, Stability of zeolites in hot liquid water, J. Phys. Chem. C 114 (2010) 19582–19595.
[18] S. Prodinger, M.A. Derewinski, Recent progress to understand and improve zeolite stability in the aqueous medium, Petrol. Chem. 60 (2020) 420–436.
[19] C. Wang, X. Liu, N. Keser Demir, J.P. Chen, K. Li, Applications of water stable metal–organic frameworks, Chem. Soc. Rev. 45 (2016) 5107–5134.
[20] M. Ding, X. Cai, H.-L. Jiang, Improving MOF stability: approaches and applications, Chem. Sci. 10 (2019) 10209–10230.
[21] L.N. McHugh, M.J. McPherson, L.J. McCormick, S.A. Morris, P.S. Wheatley, S. J. Teat, D. McKay, D.M. Dawson, C.E.F. Sansome, S.E. Ashbrook, C.A. Stone, M. W. Smith, R.E. Morris, Hydrolytic stability in hemilabile metal–organic frameworks, Nat. Chem. 10 (2018) 1096–1102.
[22] N.C. Burtch, H. Jasuja, K.S. Walton, Water stability and adsorption in metal–organic frameworks, Chem. Rev. 114 (2014) 10575–10612.
[23] A.J. Howarth, Y. Liu, P. Li, Z. Li, T.C. Wang, J.T. Hupp, O.K. Farha, Chemical, thermal and mechanical stabilities of metal–organic frameworks, Nat. Rev. Mater. 1 (2016), 15018.
[24] S. Yuan, L. Feng, K. Wang, J. Pang, M. Bosch, C. Lollar, Y. Sun, J. Qin, X. Yang, P. Zhang, Q. Wang, L. Zou, Y. Zhang, L. Zhang, Y. Fang, J. Li, H.-C. Zhou, Stable metal–organic frameworks: design, synthesis, and applications, Adv. Mater. 30 (2018), 1704303.

[25] X. Han, L. Wang, J. Li, X. Zhan, J. Chen, J. Yang, Tuning the hydrophobicity of ZSM-5 zeolites by surface silanization using alkyltrichlorosilane, Appl. Surf. Sci. 257 (2011) 9525–9531.
[26] P.A. Zapata, J. Faria, M.P. Ruiz, R.E. Jentoft, D.E. Resasco, Hydrophobic zeolites for biofuel upgrading reactions at the liquid–liquid interface in water/oil emulsions, J. Am. Chem. Soc. 134 (2012) 8570–8578.
[27] P.A. Zapata, Y. Huang, M.A. Gonzalez-Borja, D.E. Resasco, Silylated hydrophobic zeolites with enhanced tolerance to hot liquid water, J. Catal. 308 (2013) 82–97.
[28] S. Yang, L. Peng, D.T. Sun, M. Asgari, E. Oveisi, O. Trukhina, S. Bulut, A. Jamali, W. L. Queen, A new post-synthetic polymerization strategy makes metal–organic frameworks more stable, Chem. Sci. 10 (2019) 4542–4549.
[29] A. L'Hermitte, D.M. Dawson, P. Ferrer, K. Roy, G. Held, T. Tian, S.E. Ashbrook, C. Petit, Formation mechanism and porosity development in porous boron nitride, J. Phys. Chem. C 125 (2021) 27429–27439.
[30] T. Furuta, M. Sakai, T. Isobe, A. Nakajima, Negative line tension for an ionic liquid on a hydrophobic fluoroalkylsilane coating, Chem. Lett. 38 (2009) 1092–1093.
[31] L. Greenspan, Humidity fixed points of binary saturated aqueous solutions, J. Res. Natl. Bur. Stand. A Phys. Chem. (1977) 89–96.
[32] D. Bahamon, L.F. Vega, Systematic evaluation of materials for post-combustion CO_2 capture in a temperature swing adsorption process, Chem. Eng. J. 284 (2016) 438–447.
[33] M.H.N. Yio, Y.W. Ho, F. Abdul Wahid, H.S. Wong, N.R. Buenfeld, Analysis of cement paste and aggregate content of concrete using micro X-ray fluorescence, Mag. Concr. Res. 74 (2022) 889–904.
[34] J.W.M. Osterrieth, J. Rampersad, D. Madden, N. Rampal, L. Skoric, B. Connolly, M. D. Allendorf, V. Stavila, J.L. Snider, R. Ameloot, J. Marreiros, C. Ania, D. Azevedo, E. Vilarrasa-Garcia, B.F. Santos, X.H. Bu, Z. Chang, H. Bunzen, N.R. Champness, S. L. Griffin, B. Chen, R.B. Lin, B. Coasne, S. Cohen, J.C. Moreton, Y.J. Colón, L. Chen, R. Clowes, F.X. Coudert, Y. Cui, B. Hou, D.M. D'Alessandro, P.W. Doheny, M. Dincă, C. Sun, C. Doonan, M.T. Huxley, J.D. Evans, P. Falcaro, R. Ricco, O. Farha, K.B. Idrees, T. Islamoglu, P. Feng, H. Yang, R.S. Forgan, D. Bara, S. Furukawa, E. Sanchez, J. Gascon, S. Telalović, S.K. Ghosh, S. Mukherjee, M. R. Hill, M.M. Sadiq, P. Horcajada, P. Salcedo-Abraira, K. Kaneko, R. Kukobat, J. Kenvin, S. Keskin, S. Kitagawa, K.i. Otake, R.P. Lively, S.J.A. DeWitt, P. Llewellyn, B.V. Lotsch, S.T. Emmerling, A.M. Pütz, C. Martí-Gastaldo, N. M. Padial, J. García-Martínez, N. Linares, D. Maspoch, J.A. Suárez del Pino, P. Moghadam, R. Oktavian, R.E. Morris, P.S. Wheatley, J. Navarro, C. Petit, D. Danaci, M.J. Rosseinsky, A.P. Katsoulidis, M. Schröder, X. Han, S. Yang, C. Serre, G. Mouchaham, D.S. Sholl, R. Thyagarajan, D. Siderius, R.Q. Snurr, R. B. Goncalves, S. Telfer, S.J. Lee, V.P. Ting, J.L. Rowlandson, T. Uemura, T. Iiyuka, M.A. van der Veen, D. Rega, V. Van Speybroeck, S.M.J. Rogge, A. Lamaire, K. S. Walton, L.W. Bingel, S. Wuttke, J. Andreo, O. Yaghi, B. Zhang, C.T. Yavuz, T. S. Nguyen, F. Zamora, C. Montoro, H. Zhou, A. Kirchon, D. Fairen-Jimenez, How reproducible are surface areas calculated from the BET equation? Adv. Mater. 34 (2022).
[35] S. Brunauer, P.H. Emmett, E. Teller, Adsorption of gases in multimolecular layers, J. Am. Chem. Soc. 60 (1938) 309–319.
[36] H. Azzan, A.K. Rajagopalan, A. L'Hermitte, R. Pini, C. Petit, Simultaneous estimation of gas adsorption equilibria and kinetics of individual shaped adsorbents, Chem. Mater. 34 (2022) 6671–6686.
[37] R. Pini, Interpretation of net and excess adsorption isotherms in microporous adsorbents, Microporous Mesoporous Mater. 187 (2014) 40–52.
[38] J.D. Evans, V. Bon, I. Senkovska, S. Kaskel, A universal standard archive file for adsorption data, Langmuir 37 (2021) 4222–4226.
[39] G. Socrates, Infrared and Raman Characteristic Group Frequencies: Tables and Charts, third ed., Wiley, Chichester, 2001.
[40] P.J.E. Harlick, A. Sayari, Applications of pore-expanded mesoporous silicas. 3. Triamine silane grafting for enhanced CO_2 adsorption, Ind. Eng. Chem. Res. 45 (2006) 3248–3255.
[41] A. Ulman, Formation and structure of self-assembled monolayers, Chem. Rev. 96 (1996) 1533–1554.
[42] O.O. Kurakevych, V.L. Solozhenko, Rhombohedral boron subnitride, $B_{13}N_2$, by X-ray powder diffraction, Acta Crystallogr. C 63 (2007) i80–i82.
[43] E. Glueckauf, Theory of chromatography. Part 10.—formulæ for diffusion into spheres and their application to chromatography, Trans. Faraday Soc. 51 (1955) 1540–1551.